Sustainable Energy & Fuels

Numerical Monte Carlo Simulations of Charge Transport across the Surface of Dye and Cocatalyst Modified Spherical Nanoparticles under Conditions of Pulsed or Continuous Illumination

Journal:	*Sustainable Energy & Fuels*
Manuscript ID	SE-ART-01-2019-000009
Article Type:	Paper
Date Submitted by the Author:	05-Jan-2019
Complete List of Authors:	Tkaczibson, Kevin; University of California, Materials Science & Engineering Ardo, Shane; University of California, Chemistry; University of California, Materials Science & Engineering; University of California, Chemical & Biomolecular Engineering

Numerical Monte Carlo Simulations of Charge Transport across the Surface of Dye and Cocatalyst Modified Spherical Nanoparticles under Conditions of Pulsed or Continuous Illumination

Kevin Tkaczibson[1] and Shane Ardo[1,2,3]

[1]Department of Materials Science & Engineering, [2]Department of Chemistry, [3]Department of Chemical & Biomolecular Engineering, University of California Irvine, Irvine, CA 92697-2025 USA

Abstract

Solar fuels constructs consisting of discrete light-absorbers and distinct redox-active electrocatalysts are well-suited for numerical modeling of their charge-transfer processes. Herein by several series of Monte Carlo simulations employing spherical nanoparticle molecular supports, we identify conditions that result in the largest yield for forming specific redox states of electrocatalysts. In general, the yield for electrocatalyst oxidation/reduction increased as the self-exchange electron-transfer time constant decreased and/or the recombination time constant increased. When the number of electrocatalysts increased to more than one per nanoparticle, yields for oxidation/reduction of electrocatalysts decreased because oxidative/reductive equivalents were diluted among the larger number of electrocatalysts. As the light intensity increased the yield for oxidation/reduction of electrocatalysts again increased both in absolute number and yield per absorbed photon. However, at extreme photon fluences the yield per absorbed photon decreased due to significantly faster recombination manifest from the equal-concentration second-order nature of the recombination reaction in the number of oxidized/reduced molecules per nanoparticle. Results obtained using electrocatalysts that only required a single oxidation/reduction event for turnover were within error the same irrespective of whether optical excitation was simulated to occur as an initial pulse, to mimic pulsed-laser spectroscopic measurements, or with repeated photoexcitation events, to mimic conditions of solar illumination. However, when electrocatalysts required multiple oxidations/reductions for turnover the intensity of pulsed light required to obtain the same electrocatalyst turnover yield that we observed using repeated photoexcitation depended greatly on the electron-transfer time constants. In addition, at

solar-relevant fluences the equal-concentration second-order kinetic process for recombination exhibited a first-order dependence on the number of nanoparticles that contained an oxidized/reduced molecule. The rate of electrocatalyst turnover after two redox events was also determined to have a first-order dependence in the concentration of oxidized/reduced molecules over most of the transient. Collectively the solar-simulated data showed that even under the assumption of ideal kinetic processes and molecular and semiconductor densities of states, the observed kinetic behavior can be complex and change as a function of time and fluence. These observations suggest that results from pulsed-laser spectroscopic measurements are not always accurate predictors of the expected behavior of sunlight-illuminated dye-sensitized photoelectrochemical cells that drive multiple-charge-transfer reactions.

Introduction

Designing and evaluating architectures for solar fuels generation are worthwhile academic research endeavors that may one day lead to an economically pertinent technology that enables long-term seasonable energy storage and/or a transportation fuel.[1–5] This type of energy storage is predicted to be necessary when society is powered by substantial renewable energy.[5] Architectures for solar fuels constructs generally fall into several broad categories. The most efficient designs consist of photovoltaic-grade materials with buried-junctions for effective photovoltaic action and that are protected from corrosion using chemically insulating overlayer coatings or direct electrical wiring to aqueous electrolytes where materials electrocatalysts perform the electrochemical reactions.[3,6–11] Other designs rely on coupled processes that together are much less well understood and often occur at semiconductor–liquid junctions with or without molecular electrocatalysts and/or dye sensitizers.[12–31] Each of these constructs has benefited from experimental and computational studies of its photophysical and photochemical processes in order to elucidate mechanistic details of operation and identify architectures that result in large power-conversion efficiencies.

Several types of computational models have been used to simulate and assess the performance limitations of solar fuels constructs. Some models capture bulk collective dynamics and overall photovoltaic performance using statistical ensemble models. For example, limiting physical processes in buried-junction designs and non-molecular photoelectrochemical designs have been

simulated successfully using coupled differential equations that capture deterministic behaviors expected from statistical thermodynamics.[4,32–34] For mesoporous dye-sensitized designs, transport phenomena for redox-active species in solution and rates of electron transport between dyes and within mesoporous thin films have been modeled using various methods with numerical results that are reasonably consistent with experimental observations.[35–44] However, a limitation of simulations that capture continuous and/or bulk behaviors is that they lack the granularity required to capture dynamics that occur at discrete molecular light absorbers and electrocatalysts. The molecularity of these photochemical designs can be studied using ab initio quantum calculations, density functional theory, electronic structure determination, and molecular dynamics simulations. However, these atomic-level calculations are too fine-grained to capture dynamics that occur across nanometer-to-micron-sized regions consisting of hundreds to thousands of molecules that are critical in order to predict the overall function of the materials system. A modeling domain that is intermediate between these two size regimes is required to capture the micro-kinetic behavior of these systems on pertinent size scales. This need motivated us to develop a physically pertinent numerical modeling and simulation package based on a discrete-time random walk Monte Carlo method and that we will share publicly. It is the first of its kind that captures salient features of dye-sensitized and cocatalyst-modified constructs with the aim to help guide and progress the design of these systems to a practical level of device viability.

An enormous number of fundamental experiments have been conducted on dye-sensitized mesoporous thin films using a broad range of techniques.[45,46] To better understand observed behaviors related to charge transfer, Monte Carlo simulations have been performed that simulate Markovian micro-kinetic processes and quantify rates of electron and energy transfer between dyes only.[45,47] Some of the initial work was reported by Meyer and colleagues in the early 2000s, who modeled surface transport processes via classical *discrete-time* random walk Monte Carlo simulations across a two-dimensional lattice with periodic boundary conditions.[48] Around the same time, Nelson, Durrant and colleagues introduced a mathematically rigorous model for charge recombination from these TiO_2 nanocrystallites to surface-bound dyes based on a *continuous-time* random walk model.[42,49–52] A critical assumption in this type of random walk model is that the walkers are independent and also that the location of the oxidized dye does not change appreciably on the timescale of the recombination process, which is not often a valid assumption.[37,53–62] Since that time, additional random walk Monte Carlo models have been reported for analogous processes

and using computer code with similar features and limitations as first reported in the early 2000s.[41,63–67] In 2009, Ardo and Meyer were the first to incorporate specifically three-dimensional spherical nanoparticle supports into discrete-time random walk models, thus removing the need for periodic boundary conditions.[58,59] This was an important advance that remedied the non-physical limitation of the two-dimensional simulations, which occurred because in two-dimensions, regions on the particles near the poles (top/bottom) inherently had an excess number of molecular positions that incorrectly weighted processes in those region. Moreover, the two-dimensional models did not allow for accurate quantification of the spherical polar angular position of the molecules in three dimensions. This spatial information is needed for each perturbed dye in order to accurately model experimental data obtained from time-resolved polarization spectroscopy techniques, which can be used to quantify rates of transport across surfaces such as self-exchange electron transfer or energy transfer across nanometer-scale particles and on the nanosecond and longer timescales.[58,59] Since then other discrete-time random walk models have incorporated three-dimensional semiconductor nanoparticles[60,61,68,69] and even included surface-confined charge transport across interparticle necking regions.[67,70] Interparticle charge transport is an important process that captures dynamics occurring over the scale of several semiconductor nanoparticles. While our code is also able to model and simulate interparticle charge transport behavior, herein for our initial studies we do not incorporate this feature because the model parameter space is rich enough in its absence. Unique to our model, in comparison to all other prior models,[45,47,71,72] is that we identify kinetic parameters that lead to the most effective utilization of photons *for turnover of multiple-electron-transfer cocatalysts* under the simulated condition of pulsed-light excitation *or continuous illumination*. We report results from a series of parametric time-inhomogeneous random walk Monte Carlo simulation studies using isolated spherical nanoparticles arranged as a stack to mimic their spatial location as a thin film. These results are highly pertinent to dye-sensitized cocatalyst-modified semiconductor nanoparticles that constitute mesoporous photoelectrochemical electrodes or consist of colloidal suspensions.

Experimental

Modeling Framework. The architecture modeled is motivated by mesoporous thin films of nanoparticles that are commonly used in dye-sensitized photoelectrochemical constructs, where

nominally identical spherical anatase TiO_2 nanocrystallites contain discrete surface-anchored light-absorbing moieties and redox-active electrocatalysts (Figure 1). In the case of traditional dye-sensitized materials, both the light-absorbers and the electrocatalysts are molecules, but the model is general in that, for example, the light-absorbing units could be surface-confined material units like quantum dots or nanocrystalline regions with isolated optical transitions in the solid-state, or the electrocatalysts could be materials whose charge localization and transport follows a hopping or polaronic transport mechanism.[73] The model is able to simulate discrete processes that spatially exchange states, such as self-exchange Dexter or Förster energy transfer or self-exchange electron transfer initiated at an oxidized or reduced dye. Self-exchange electron transfer is the process assumed for the simulations performed herein with hops to only the closest adjacent dyes being possible, which is a valid assumption based on reasonable conditions and prior analyses.[74] The structure is incorporated into the model as 100 spheres that are positioned optically in series as a one-dimensional stack but that do not physically interact. The top sphere in this stack is considered to be at the surface of the thin film with subsequent spheres further down from the surface, at larger z-coordinates. The surfaces of these spheres are tessellated as icosahedra, using Wolfram Mathematica's built-in "Geodesate" function, which results in approximately evenly spaced points that represent possible locations of molecules. By tessellating 5 icosahedra, 252 points were generated on the surface of the sphere, with 240 hexagonally packed (6 adjacent points), and the remaining 12 pentagonally packed (5 adjacent points). It was not necessary to specifically identify the nanoparticle radius, molecule radius, film thickness, and film porosity, because they are all related and so only their relative sizes are pertinent. However, based on the values chosen for the number of locations for molecules per particle (252), the number of particles per stack (100), and the use of a stack to model a mesoporous film of ~50% porosity, the geometry is consistent with characteristics of typical dye-sensitized mesoporous TiO_2 thin films.[60,74,75]Per particle, a specific

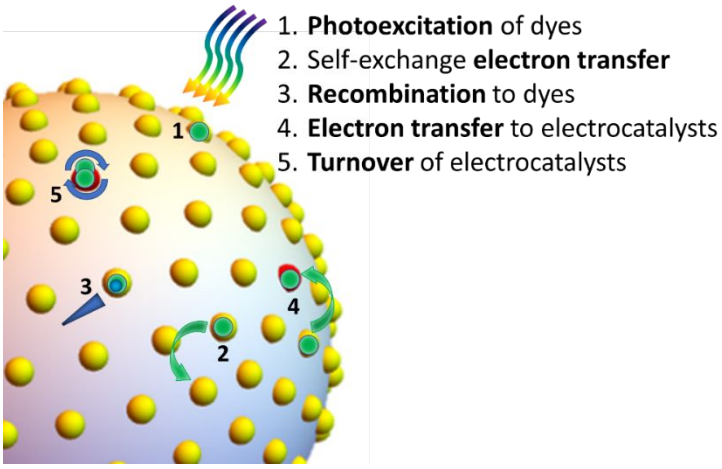

Figure 1. Model schematic showing the events that are included in the model to mimic the major kinetic processes that are operative in actual dye-sensitized photoelectrochemical constructs.

number of these 252 points was chosen as positions of electrocatalysts that could be oxidized/reduced once or multiple times. Multiple transfers are desired in practical applications that make and break stable chemical bonds via multiple-electron/proton-transfer reactions. The position of each electrocatalyst on a single particle was chosen at random, with an additional option to evenly distribute the electrocatalysts over each particle such that each particle had the same number of electrocatalysts. The remaining points were chosen to be dyes, and based on the pulsed photon fluence chosen for the experiment, locations for initial photoexcitation were chosen as a subset of dye positions. All simulations assumed unity quantum yield for rapid excited-state electron transfer between photoexcited dyes and the semiconductor support, such that photoexcitation always resulted in an oxidized/reduced dye molecule. For each semiconductor nanoparticle, its number of mobile electrons/holes was set equal to the number of oxidized/reduced molecular charges on its surface; however the transport processes of the electrons/holes were not simulated. *Information regarding generation of initial conditions are described in more detail below.* The simulation proceeded by randomly choosing from a series of options at each timestep, including self-exchange electron transfer between two adjacent dyes or electrocatalysts, electron-transfer recombination between the semiconductor nanoparticle and an oxidized/reduced dye or electrocatalyst, photoexcitation of a ground-state dye – when conditions of continuous illumination were simulated – or doing nothing. When an electrocatalyst reached a redox state required for an electrocatalytic turnover event, the electrocatalyst was immediately regenerated and the same number of charges in the semiconductor nanoparticle were removed to simulate their collection elsewhere in the system. This occurred repeatedly until all charge-separated states either recombined or drove electrocatalysis. *Information regarding this simulation loop and the resulting output data are described in more detail below.*

Generation of Initial Conditions. Initial assignment of photoexcited dyes, and therefore charge separated dyes, was performed multiple ways depending on the desired simulated condition. A set number of photoexcited dyes was either distributed over the entire stack or placed on each particle in the stack, e.g. for the case of 200 photoexcitations over the 100-particle stack ($<n_{pe}> = 2$), either 2 dye positions were chosen randomly per particle or 200 particle numbers and dye positions were chosen randomly across the entire stack. The assignment was made using weights incorporated via an assignment matrix, with weights based on one or more geometric considerations. One option for the assignment matrix was a Beer–Lambert law generation profile,

$$W_{\mathrm{BL}} = 10^{-\frac{n}{N}(\mathrm{Abs})} = 10^{\frac{n}{N}\log_{10}(T)} \quad (1)$$

where the probability of photoexcitation decreases exponentially as the position of the dye is deeper in the stack, W_{BL} is the weight associated with a given position from the Beer–Lambert law weighting function and ranges from 0 to 1, n is the particle number in the stack, N is the total number of particles, Abs is the absorbance of the entire particle stack, and T is the fraction of transmitted light through the entire particle stack. As such, molecular positions closer to the top of the particle stack were more likely to be photoexcited. This assignment, if repeated a statistically significant number of times, yields a distribution of excited dyes that follows an exponential decay with particle height, as predicted by the Beer–Lambert law (Figure S1). Another independent option for the assignment matrix was based on polarized light excitation and well-defined radial transition dipole moments for the surface-anchored dyes. This assignment weighs each position based on the inclination angle of the dye relative to the electric field vector of the polarized excitation light,

$$W_{\mathrm{A}} = (\cos^2\theta)(\sin\theta) \quad (2)$$

where W_{A} is the weight associated with a given position from the anisotropy weighting function and θ is the angle between the normal from the center of a particle and the molecular position on its surface and the electric field vector of the polarized excitation light. Prior to performing the simulations, a list of data for each electrocatalyst, dye, and oxidized dye was generated that contained relevant parameters including molecule type (dye or electrocatalyst), recombination probability, hopping probability, oxidation state, and an array of positions for 5 or 6 adjacent molecules. Adjacent molecules were within 2.5 times the center-to-center distance between molecules the size of $[Ru^{II}(bpy)_3]^{2+}$ when in van der Waals contact. The recombination probability was set to be the same for electron transfer between the semiconductor and either an oxidized/reduced dye or an electrocatalyst. Also, when an oxidized/reduced dye is adjacent to an electrocatalyst, the hopping probability to the electrocatalyst was set to effectively 90%. *This latter point is described in more detail below.* These hopping and recombination probabilities were calculated from time constants ranging from 40 ns to 800 μs in steps of three points on a logarithmic scale. For each nanoparticle, the probability of recombination was scaled by the number of charges in that semiconductor nanoparticle. A second list of information was generated

that was updated at each Monte Carlo iteration during the simulation, which included the two-dimensional coordinates for all molecules that were altered from their initial state as (particle number, position number). At time zero this list only contained the locations of dyes that were initially photoexcited; as the initially photoexcited dyes became altered from their initial state over time these coordinates were replaced by those of other dyes or electrocatalysts.

Simulation Loop. After initially defining the state of the system at time equal to zero, Monte Carlo simulations were performed by looping over the list of molecules that were altered from their initial state (second list). For each, a probability, P_x, was assigned that ranged from 0 to 1 for the possible options of recombination, hopping to an adjacent point, or doing nothing, and with probabilities defined as follows,

$$P_x = \frac{t_{\text{step}}}{\tau_x} \tag{3}$$

where t_{step} is the amount of time between time points and τ_x is the ensemble average time constant for the process, x. At the end of each simulated timestep, the list of molecules was altered from its prior state and then the Monte Carlo process was repeated, assuming that a small and predefined timestep had passed. The value of the timestep varied and was chosen for each condition so that P_x as a percentage was < 1.1% for self-exchange electron transfer between dyes and was < 0.3% for recombination to oxidized/reduced dyes or electrocatalysts. The value of the timestep resulted in the probability of transferring a charge from an oxidized/reduced dye to an adjacent electrocatalyst being ~30%. This probability was set to be 27 times greater than the probability of transferring a charge between adjacent dyes via a self-exchange reaction in order to reflect the reasonable condition that electron transfer to/from an oxidized/reduced dye from/to an electrocatalyst is thermodynamically favorable and thus much more probable. The exact 27-times-greater probability was chosen such that there was exactly a 90% probability this would occur after an oxidized/reduced dye on hexagonally packed sites became adjacent to an electrocatalyst, with a nominally lower probability of occurring on pentagonally packed sites. (The derivation of this probability is included in the Supporting Information.) This Monte Carlo process was repeated until no oxidized/reduced dyes remained. Specific parameters used for various model inputs are listed in Table S1. An additional option in the model was its ability to mimic conditions of continuous illumination, which incorporated repeated light excitation events. The initial number of photoexcited dyes was set to zero and after each timestep there was an additional probability

for photoexcitation that scaled based on the desired intensity of solar illumination and was weighted according to the assignment matrix calculated from the Beer–Lambert Law and polarization considerations. Simulations using the condition of continuous illumination were terminated after 25,000,000 iterations and all data was used to calculate time-averaged steady-state values. While these values included the initial data prior to reaching a steady-state condition, its influence on the average values was insignificant because its inclusion only resulted in a $< 0.25\%$ change in the value, on average.

Output Data. During the simulation the number of times that an electrocatalyst is *completely* oxidized/reduced by a dye is recorded, because assuming rapid rates of electrocatalysis it is the most useful parameter to quantify the effectiveness that a condition drives solar photochemical transformations. Using these data we calculated the yield for electrocatalyst turnover, i.e. the percentage of photoexcitations that contributed to turnover of an electrocatalyst due to product formation. Photoexcitations that contributed to electrocatalyst oxidation/reduction but did not result in electrocatalyst turnover did not count toward this total. To reduce computation time, photoexcitations that were not able to contribute to electrocatalyst turnover were identified and removed from the simulations before any timesteps had been performed. This occurred when a photoexcited dye was on a nanoparticle that either had zero electrocatalysts on its surface or had fewer photoexcited dyes than the maximum oxidation/reduction state of an electrocatalyst. When these photoexcited dyes were removed, they were counted as being unproductive toward electrocatalyst turnover. Data were collected under a wide range of starting conditions including varied maximum redox state of the electrocatalysts, number of electrocatalysts, initial excitation fluence (i.e. number of initially excited dyes), use of a Beer–Lambert law distribution when assigning dye photoexcitations throughout the stack, self-exchange electron-transfer time constant between adjacent molecules, and electron-transfer recombination time constant between surface-anchored molecules and photo-generated charges in the semiconductor support.

Results and Discussion

General simulation conditions and data interpretation for the base case. For each specific condition simulated herein, electrocatalyst turnover yield (as a percentage) is reported as a function of 1 of 14 logarithmically-spaced hopping time constants, 1 of 14 logarithmically-spaced

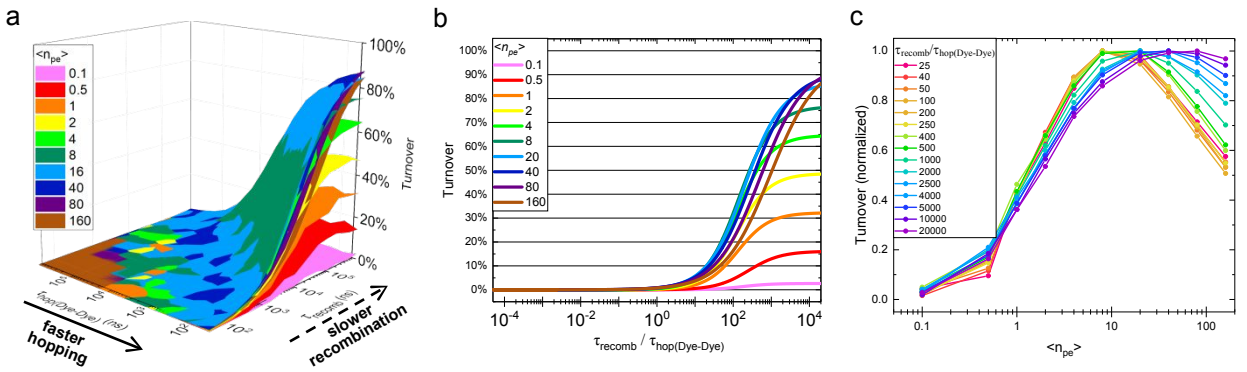

Figure 2. (a) Sheet plots representing the percentage of photoexcited dyes that ultimately *contribute to double oxidation/reduction of an electrocatalyst and turnover*, when electrocatalysts are present at 1% surface coverage at the indicated initial pulsed-light excitation fluences. (b) Non-linear least squares sigmoidal best-fits of the data in panel a as a function of the ratio of the recombination time constant to the hopping time constant. (c) Plot of the data in panel a as a function of the initial pulsed-light excitation fluence at the indicated ratio of the recombination time constant to the hopping time constant.

recombination time constants, and 1 of up to 10 logarithmically-spaced initial excitation fluences. These fluences are quantified as the average number of photoexcitations per particle over the stack of 100 particles and so a fluence of $<n_{pe}> = 2$ means that there were on average 2 photoexcitations per particle, or 200 photoexcitations created over the stack of 100 particles. Each combination of parameters for these three variables was simulated 25 times, and therefore 2500 semi-independent particles were analyzed resulting in a total of 250 – 400,000 photoexcited dyes being averaged per condition. The particles are semi-independent in that electron transfer did not occur between molecules on separate particles, but photoexcitation that followed the Beer–Lambert law generated an unequal number of initially photoexcited dyes on each particle such that particles nearer to the top of the film had more oxidized/reduced dyes while those farther from the top of the film had fewer oxidized/reduced dyes.

The data presented are reported as three-dimensional contour plots, one for each excitation fluence, as a function of the hopping time constant and recombination time constant (Figure 2a). The base case model used to obtain the data shown in Figure 2 included polarized Beer–Lambert law weighting to assign a distribution of photoexcited dyes, and electrocatalysts that could be maximally oxidized/reduced twice and occupied 1% of the possible molecular positions. Each three-dimensional contour plot for this condition changes monotonically as values on either axis increase, and therefore a series of single-fluence contour plots can easily be visualized as a series of three-dimensional sheet that spans all possible hopping and recombination time constants. This method of data visualization helps one identify the optimal fluence for ranges of kinetic

parameters, as evidenced by sheet crossover. An example of this is the band of green shown crossing through the light blue sheet in Figure 2a as the turnover yield sharply increases. Visualizing the range of kinetic parameters that leads to band formation, i.e. crossing of two sheets, can provide insights into differences in nearly identical monotonic behavior. However, it is also apparent from Figure 2a that turnover yields are nearly the same for each ratio of the recombination time constant to the hopping time constant and thus, the observed independent variable is not the hopping time constant and/or the recombination time constant but can instead be their ratio. This means that a two-dimensional plot that captures the overall effect represented by the sheets can be generated using the recombination-to-hopping time-constant ratio as the independent variable. This is shown as two-dimensional plots in Figure 2b, which were obtained by recasting all points for each sheet shown in Figure 2a with the recombination-to-hopping time-constant ratio as the independent variable and fitting the data using non-linear least-squares to a sigmoidal function (R^2 > 0.975, except for the case of $<n_{pe}>$ = 0.1 which resulted in poor signal to noise). As fluence increases from $<n_{pe}>$ = 0.1 to $<n_{pe}>$ = 8, the maximum turnover yield increases monotonically but maintains the same functional form. From $<n_{pe}>$ = 8 up to the maximum of $<n_{pe}>$ = 160, the steep portion of the sigmoidal fit shifts to larger recombination-to-hopping time-constant ratios but still reaches the same maximum turnover yield. Larger recombination-to-hopping time-constant ratios are optimal because hopping is critical to electrocatalyst turnover while recombination is detrimental. The maximum turnover yield is only ~90%, because ~10% of dye photoexcitations occur on particles containing zero electrocatalysts based on the fact that electrocatalysts are distributed randomly at an average of 1% coverage per particle.

The two-dimensional plots shown in Figure 2b report the turnover yield as a function of the ratio of the kinetic parameters, and they span the range of excitation fluences. A variation on Figure 2b is shown in Figure 2c, where the parameters are rearranged so that the normalized turnover yield is reported as a function of the excitation fluence, and they span the range of ratios of the kinetic parameters where hopping is more probable than recombination. It is apparent from these data that an intermediate fluence is ideal for each specific recombination-to-hopping time-constant ratio. The generally downward concave shape to the data occurs because the complete twice-oxidation/reduction of each electrocatalyst is less likely to occur at low fluence while the equal-concentration second-order recombination behavior is more detrimental to the turnover yield at high fluence. However, even though these data show that higher fluences result in a smaller relative

value for turnover yield, the overall rate of turnover events still increases at higher fluences, as seen in Figure S2. Also, as the recombination-to-hopping time-constant ratio increases, the optimal fluence, indicated by the global maximum of the data, decreases slightly and then greatly increases because recombination is relatively slow and therefore equal-concentration second-order recombination does not outcompete photoexcitation until large fluences are used.

Effect of electrocatalyst behavior. To understand the role that the redox state required for electrocatalyst turnover plays in the outcomes of the simulations, we performed simulations using electrocatalysts that each required only a single redox event for turnover (Figure 3). The general trends observed are very different than those observed for electrocatalysts requiring two redox events for turnover (Figure 2). For example, at lower fluences the probability of electrocatalyst turnover is small when it requires two redox events for turnover (Figure 2a,b, in pink) whereas the probability can be large when a single redox event is required for electrocatalyst turnover (Figure 3a,b, in pink). This drastically different behavior occurs at low fluences, because many photoexcitation events occur on particles where there are too few oxidized/reduced dyes to perform multiple redox reactions with any given electrocatalyst. As the fluence increases, photoexcitations become concentrated enough that they are reliably created in sufficient numbers to oxidize/reduce electrocatalysts once or twice as needed for turnover. However, then the limitation in turnover yield is the ratio τ_{recomb} / $\tau_{hop(Dye–Dye)}$, where faster relative rates of hopping (small $\tau_{hop(Dye–Dye)}$) are more beneficial to turnover yield (Figure 2b and Figure 3b), as described above. Another notable difference that arises from decreasing the number of redox events required for electrocatalyst

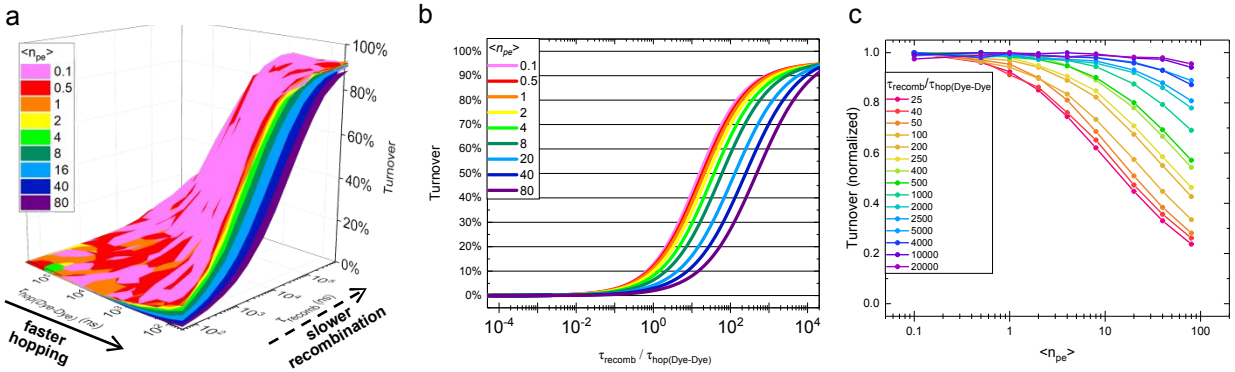

Figure 3. (a) Sheet plots representing the percentage of photoexcited dyes that ultimately *contribute to single oxidation/reduction of an electrocatalyst and turnover*, when electrocatalysts are present at 1% surface coverage at the indicated initial pulsed-light excitation fluences. (b) Non-linear least squares sigmoidal best-fits of the data in panel a as a function of the ratio of the recombination time constant to the hopping time constant. (c) Plot of the data in panel a as a function of the initial pulsed-light excitation fluence at the indicated ratio of the recombination time constant to the hopping time constant.

turnover is shown in Figure 3c versus Figure 2c. Unlike the case when each electrocatalyst requires two redox events for turnover, single redox events at electrocatalysts are most likely to occur at the lowest fluences. At very high fluences, the relative turnover yield is small irrespective of the redox state required for electrocatalyst turnover. This behavior is almost entirely dictated by τ_{recomb} / $\tau_{hop(Dye–Dye)}$, where faster hopping (small $\tau_{hop(Dye–Dye)}$) and slower recombination (large τ_{recomb}) are optimal and conditions of higher fluence suffer from increased rates of recombination due to it being an equal-concentration second-order kinetic process in the number of oxidized/reduced molecules per particle. In summary, low fluence is optimum when electrocatalyst turnover requires single redox events. However, when electrocatalyst turnover requires two redox events, $\langle n_{pe} \rangle \approx 10$ is optimum at small values of τ_{recomb} / $\tau_{hop(Dye–Dye)}$ and this optimal value for $\langle n_{pe} \rangle$ increases as τ_{recomb} / $\tau_{hop(Dye–Dye)}$ increases (Figure 2c).

Effect of the Beer–Lambert law. Use of the Beer–Lambert law to model the photoexcitation distribution in mesoporous thin films used in dye-sensitized solar cells is in general accurate for non-scattering films. However, to understand the influence that the photoexcitation profile has on electrocatalyst turnover we compared the condition where photoexcitation events followed a Beer–Lambert law distribution to the condition where the number of photoexcitation events was the same for each particle and therefore spatially homogeneous over the stack (Figure 4 and Figure

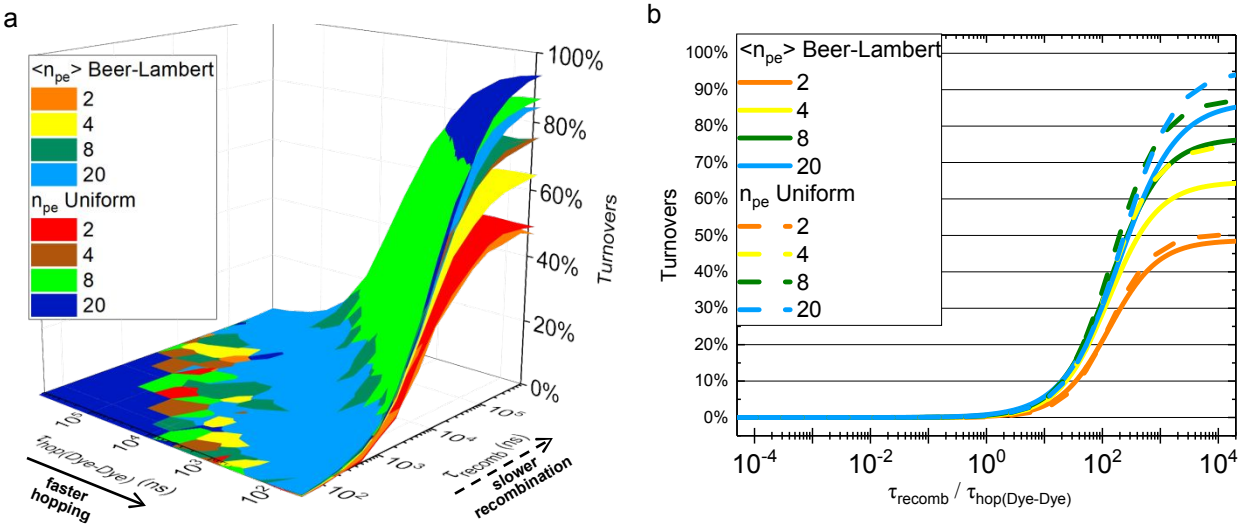

Figure 4. (a) Sheet plots representing the percentage of photoexcited dyes that ultimately contribute to double oxidation/reduction of an electrocatalyst and turnover when electrocatalysts are present at 1% surface coverage at the indicated initial pulsed-light excitation fluences *that follow the Beer-Lambert law or a uniform distribution over the stack*. (b) Non-linear least squares sigmoidal best-fits of the data in panel a as a function of the ratio of the recombination time constant to the hopping time constant.

S3, respectively). The lowest possible fluence resulting in homogenous photoexcitation events (n_{pe} = 1) resulted in only one oxidized/reduced dye per particle, and therefore a 0% chance of turnover for electrocatalysts requiring two or more redox events for turnover. In this case, use of the Beer–Lambert law distribution was beneficial. However, for all other values of $<n_{pe}>$ evaluated, turnover yield is larger when uniform photoexcitation occurs instead of using a Beer–Lambert law excitation profile. For example, Figure 4 shows nearly identical plots for the dark green sheet ($<n_{pe}>$ = 8, with Beer–Lambert law generation) and the brown sheet (n_{pe} = 4, without Beer–Lambert law generation) meaning that uniformly exciting dyes is approximately the same as having twice as many total excitations that follow a Beer–Lambert law distribution. This is because the Beer–Lambert law distribution often results in some photoexcitations that occur too sparsely to be useful and others that are so concentrated that the equal-concentration second-order nature of the recombination process results in more rapid loss of oxidized/reduced dyes. That is, toward the bottom of the stack it is likely that some photoexcitations occur on particles with no other photoexcitation events and therefore these events are never able to contribute to the two redox events required for turnover of an electrocatalyst. And at the top of the stack the rate of recombination is fast because these particles often have significantly more photoexcitations per particle than $<n_{pe}>$. Also, notably for the condition of $<n_{pe}>$ = 2, uniform photoexcitation provides little benefit over photoexcitation that follows a Beer–Lambert law distribution, because the rates of equal-concentration second-order recombination are not drastically different for particles with few photoexcitations. Collectively, these data suggest that optimal conditions include having a very thin layer of strongly-absorbing material or a thick layer of weakly-absorbing material. Alternatively, introducing scattering particles to more evenly distribute the incoming light across the stack is beneficial. Non-uniform photoexcitation is also problematic for fundamental studies of charge carrier dynamics and interfacial electron-transfer processes measured using transient absorption spectroscopy, because the ensemble kinetic behavior simultaneously reports on several simple first-order and/or second-order kinetic processes but under different initial excitation conditions. The aggregate transient absorption signal therefore not follow traditional kinetic models, which is a behavior that has been reported previously in the literature.[45,47,49–52,61]

Effect of electrocatalyst valency. The model herein shows that the yield for electrocatalyst turnover is smaller when an electrocatalyst must be oxidized/reduced twice instead of just once for turnover, a fact that is relevant to two-electron-transfer reactions like molecular dihydrogen evolution. However, many reactions require even more than two redox events for electrocatalytic turnover. For example, oxidation of water to molecular dioxygen occurs via a four electron, four proton redox reaction, and in Nature's oxygen-evolving complex this net reaction is thought to occur via a single concerted O–O bond-forming step.[76] Because of the large interest in the oxygen evolution reaction, and other reactions requiring even more redox equivalents like molecular dinitrogen reduction to ammonia (6 electrons and 6 protons) and carbon dioxide reduction to methane (8 electrons and 8 protons), we performed simulations using electrocatalysts that are capable of accumulating 1, 2, or 4 charges prior to turnover, and did so at low ($<n_{pe}> = 1$), intermediate ($<n_{pe}> = 8$), and high ($<n_{pe}> = 80$) photon fluences. Figure 5 and Figure S4 show that in order to net oxidize/reduce an electrocatalyst four times, especially large fluences are required. However, this condition is not beneficial from a recombination perspective and therefore, large values for $\tau_{recomb} / \tau_{hop(Dye–Dye)}$ are needed to observe large values for turnover yield. These data follow the trends observed in Figure 2c where there is an optimal fluence that results in the largest turnover yield when $\tau_{recomb} / \tau_{hop(Dye–Dye)}$ is large. Collectively, these data suggest that optimal fluence scales with the number of redox events required for turnover of an electrocatalyst.

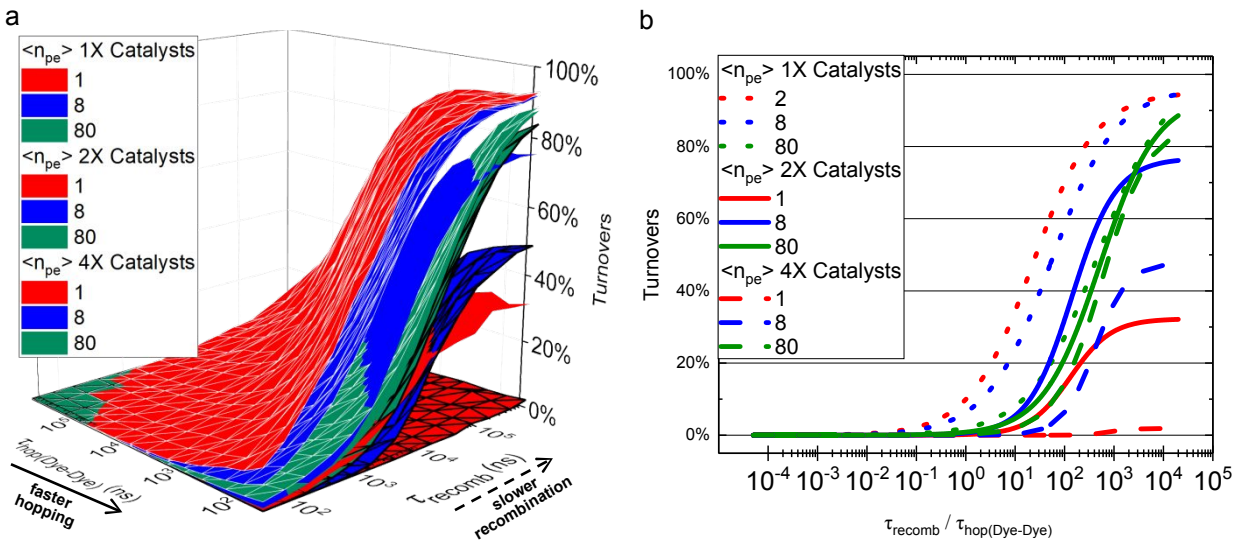

Figure 5. (a) Sheet plots representing the percentage of photoexcited dyes that ultimately *contribute to the indicated single (1X), double (2X), or quadruple (4X) oxidation/reduction of an electrocatalyst and turnover*, when electrocatalysts are present at 1% surface coverage at the indicated initial pulsed-light excitation fluences. (b) Non-linear least squares sigmoidal best-fits of the data in panel a as a function of the ratio of the recombination time constant to the hopping time constant.

Effect of electrocatalyst coverage. Another parameter evaluated was the percent of positions occupied by electrocatalysts rather than dyes. In the base case, maximally twice oxidized/reduced electrocatalysts with a 1% coverage – or on average 2.52 electrocatalysts per particle – were used, and photoexcitation events were distributed according to a Beer–Lambert law distribution. In Figure 6, this condition is used to compare effects with other electrocatalyst coverages of 0.5%, 2%, and 4%, which correspond to on average 1.26, 5.04, and 10.08 electrocatalysts per particle, respectively. While 1% electrocatalyst coverage appears to be optimal when τ_{recomb} / $\tau_{hop(Dye–Dye)}$ is large, higher coverages are optimal as τ_{recomb} / $\tau_{hop(Dye–Dye)}$ decreases. With increasing coverage of electrocatalysts, accumulation of charges at electrocatalysts is more difficult, because the same number of oxidized/reduced dyes is diluted over a larger number of electrocatalyst sites. This limits turnover yield when τ_{recomb} / $\tau_{hop(Dye–Dye)}$ is large and therefore turnover is overall ineffective when there are too many electrocatalysts in the system. These simulation results are consistent with behavior that we observed previously via pulsed-laser spectroscopy experiments.[60] If τ_{recomb} / $\tau_{hop(Dye–Dye)}$ is small such that electrocatalyst turnover is poor, dilution of charges among electrocatalysts no longer limits turnover yield and instead recombination is limiting. In these cases, having a larger coverage of electrocatalysts results in a larger turnover yield because oxidizing/reducing an electrocatalyst occurs more frequently. This is clear from the data in Figure 6 where as τ_{recomb} / $\tau_{hop(Dye–Dye)}$ increases, the optimal coverage of electrocatalysts changes from 4% (green sheet) to 2% (light green sheet) and ultimately to 1% (yellow sheet). The condition of 1% coverage of electrocatalysts remains optimal under the fluences, electrocatalyst coverages, and values of τ_{recomb} / $\tau_{hop(Dye–Dye)}$ evaluated. However, the value of τ_{recomb} / $\tau_{hop(Dye–Dye)}$ where the optimal electrocatalyst coverage changes is dependent on the fluence. At low fluence, the size of the band in the sheet plot where the 1% electrocatalyst coverage condition is optimum is largest, while the transition of 4% to 1% electrocatalyst coverage being optimum occurs over the smallest region in the figure (Figure 6a). At high fluence, τ_{recomb} / $\tau_{hop(Dye–Dye)}$ must be near-optimal in order for 1% electrocatalyst coverage to be most effective at electrocatalyst turnover, and bands for both 2% and 4% electrocatalyst coverage are large (Figure 6d). This observation is extremely pertinent to dye-sensitized photoelectrochemical constructs, where most experimental demonstrations report that low coverages of electrocatalysts lead to the largest efficiencies for light-driven oxygen evolution through water oxidation.[77] Data from our simulations suggest that when the electrocatalyst coverage is relatively large (≥ 4%), optimal performance is observed at larger

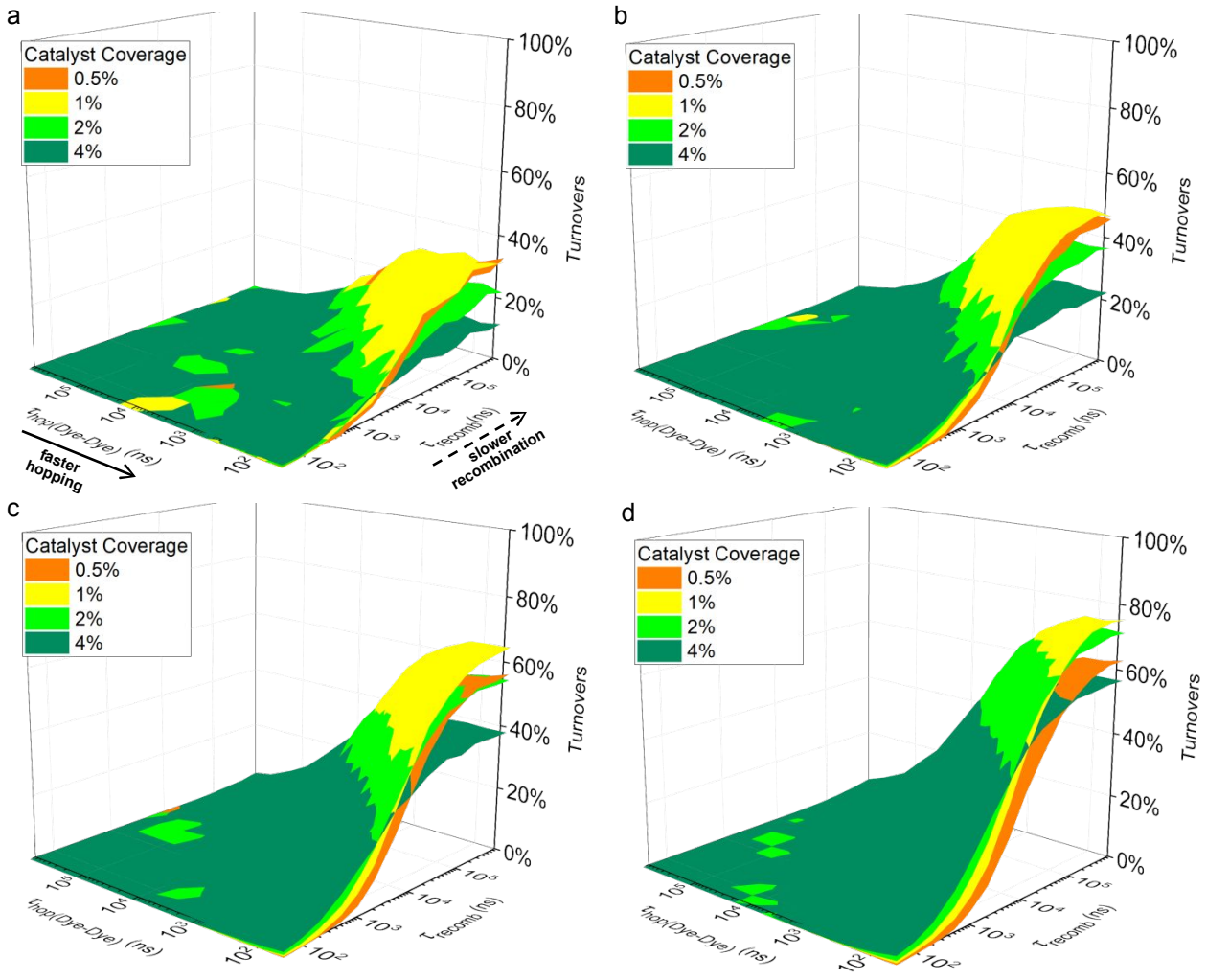

Figure 6. Sheet plots representing the percentage of photoexcited dyes that ultimately contribute to double oxidation/reduction of an electrocatalyst *when electrocatalyst are present at the indicated surface coverage* at the initial pulsed-light excitation fluence of (a) $\langle n_{pe} \rangle = 1$, (b) $\langle n_{pe} \rangle = 2$, (c) $\langle n_{pe} \rangle = 4$, or (d) $\langle n_{pe} \rangle = 8$.

fluences and large values of τ_{recomb} / $\tau_{hop(Dye–Dye)}$. However, if lower fluences are used, our data suggest that a lower coverage of electrocatalysts is optimum.

Effect of pulsed-light excitation versus continuous-wave illumination. A major challenge in using the results reported above to predict behaviors of dye-sensitized photoelectrochemical constructs is that most often efficiencies for light-driven oxygen evolution through water oxidation are measured using conditions of continuous illumination and not initial pulsed-light excitation as simulated herein. This prompted us to quantify the yield for electrocatalyst turnover during

conditions of continuous illumination, which was mathematically implemented as a probability for light excitation at each step in the Monte Carlo simulation.

In order to realize efficiency gains in dye-sensitized photoelectrochemical constructs, detailed mechanisms and quantum yields for electron, charge, and energy transfer processes are necessary. Common techniques used to probe these processes include transient-absorption spectroscopy and time-resolved photoluminescence spectroscopy.[45] However, it is not known whether these pulsed-laser pump–probe techniques can replicate behaviors observed under practical conditions of continuous-wave illumination, which is the relevant condition for actual application of these photochemical materials systems. For this reason, we modeled the effects of repeated light excitation under conditions of solar-simulated illumination for a state-of-the-art dye-sensitized solar cell (~20 mA/cm^2) but under the caveat that surface-anchored electrocatalysts are present and that each requires one, two, or four redox events for turnover to mimic common conditions required for electrocatalytic reactions. For electrocatalysts requiring a single redox event for turnover, results from repeated light excitation at intensities of effectively 1 Sun and 10 Suns are in excellent agreement with results obtained using simulated initial pulsed-light excitation at low fluences ($\langle n_{pe} \rangle$ = 0.5 – 1.0 excitations) (Figure 7a). Data obtained for conditions of effectively 100 Suns excitation were very similar to those under lower light intensities, albeit with small differences described in more detail below. When each electrocatalyst required two or more redox events for turnover, results over the same range of solar-simulated light intensities could not be reproduced by any condition utilizing initial pulsed-light excitation (Figure 7b,c). Also, it is clear

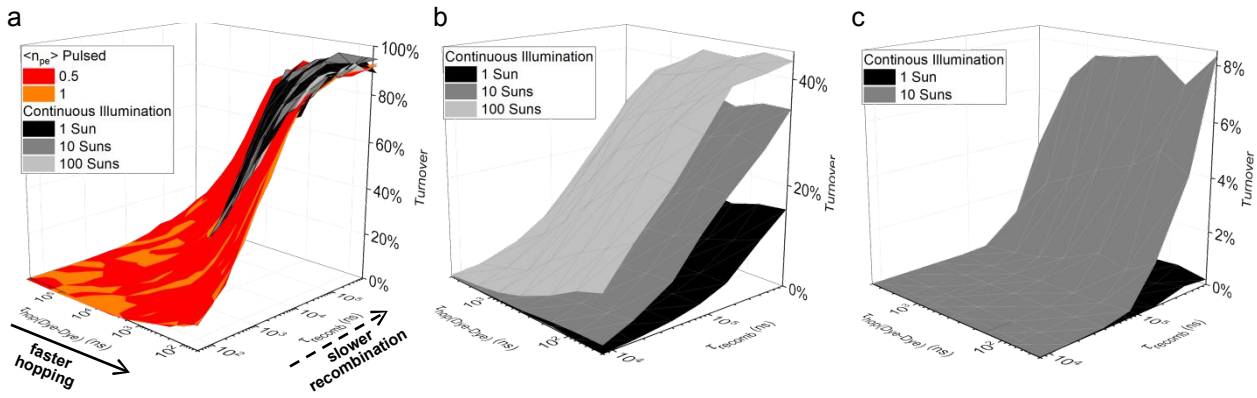

Figure 7. Sheet plots representing the percentage of photoexcited dyes that ultimately *contribute to (a) single, (b) double, or (c) quadruple oxidation/reduction of an electrocatalyst and turnover*, when electrocatalysts are present at 1% surface coverage at the indicated initial pulsed-light excitation fluences (colored sheets, taken from Figure 2) or continuous illumination solar-simulated fluences (grayscale sheets).

from these data that turnover yields are no longer the same for each value of τ_{recomb} / $\tau_{hop(Dye–Dye)}$, meaning that τ_{recomb} / $\tau_{hop(Dye–Dye)}$ is not a reasonable single independent variable for these data and that all data in a single sheet can no longer be represented by a sigmodal as a function of τ_{recomb} / $\tau_{hop(Dye–Dye)}$. The sensitivity of turnover yield to the light excitation condition depends on which time constant is varied. Starting at the optimal condition of small $\tau_{hop(Dye–Dye)}$ and large τ_{recomb}, turnover yield decreases substantially as the recombination time constant decreases; however, turnover yield is nearly constant as the hopping time constant increases. This suggests that the optimal condition is one where recombination is dictating the overall turnover yield, for electrocatalysts requiring two or four redox events for turnover (Figure 7b,c), but not for electrocatalysts requiring a single redox event for turnover (Figure 7a).

The plots shown in Figure 7 are rich in information, but interpreting them when τ_{recomb} / $\tau_{hop(Dye–Dye)}$ is not a good indicator of turnover yield is challenging. Therefore, we decided to analyze the data under conditions where one time constant is fixed while the other time constant is varied. Because of the vastly different yields for electrocatalyst turnover under large and small time constant values, we decided that this analysis should be performed for multiple values of the fixed time constants, and therefore that the perimeter of the plots shown in Figure 7 would be most instructive and representative of the overall behavior. The resulting panoramic plots were constructed by starting at the condition where turnover yield is smallest, i.e. where $\tau_{hop(Dye–Dye)}$ is largest and τ_{recomb} is smallest, and reporting turnover yield as the time constants are stepped clockwise along the perimeter of the plots in Figure 7a,b. This protocol is shown schematically as Figure S5 and the resulting plots are shown in Figure 8a,b. As expected, the plots are nearly symmetric for the condition when electrocatalysts required a single redox event for turnover (Figure 8a), however the plots are clearly asymmetric for the condition when electrocatalysts required two redox events for turnover (Figure 8b). The causes of this asymmetry are due to the complex interplay of the competing kinetic processes. To understand which kinetic processes are rate-limiting for each set of time constants, it is useful to examine the steady-state number of oxidized/reduced molecules present on the surface of the nanoparticles as a function of the intensity of repeated light excitation (Figure 8c,d and Figure S6). This is because the relationship between the number of charges present at steady-state, the photon fluence, and the recombination rate is well known based on detailed balance and Kirchhoff's current law. It follows that under steady-state conditions, per particle, the rate of generation of charges due to photon absorption (*G*

= I_{light}) equals the rate of loss of charges due to recombination and electrocatalytic turnover (R), which by mass action has the following kinetic rate law,

$$R = k_1(n_{ssc})^{v_1} + k_2(n_{ssc})^{v_2} \quad (4)$$

where k_i are the rate constants for the rate-limiting reactions, n_{ssc} is the steady-state number of charges on the nanoparticle, and the v_i are the order of the reactions in n_{ssc}. Assuming only one process with $v_i \neq 0$ dominates the loss term, R, the following log–log relation and derivative hold,

$$\log_{10}[n_{ssc}] = \frac{1}{v}\log_{10}[I_{light}] - \frac{1}{v}\log_{10}[k], \text{ and so} \quad (5a)$$

$$d(\log_{10}[n_{ssc}]) \Big/ d(\log_{10}[I_{light}]) = \frac{1}{v} \quad (5b)$$

Further analysis of this equation for the slope (Equation 5b) reveals that when the light intensity is increased by an order of magnitude, such that $d\log_{10}[I_{light}] = 1$, the following relation and ratio hold,

$$d(\log_{10}[n_{ssc}]) = \frac{1}{v} = \log_{10}[n_{ssc\_high}] - \log_{10}[n_{ssc\_low}], \text{ and so} \quad (6a)$$

$$n_{ssc\_high} \Big/ n_{ssc\_low} = 10^{\frac{1}{v}} \quad (6b)$$

where high and low stand for the relative conditions of high and low light intensity. Using Equation 6b to compare the ratio of the steady-state number of charges per particle at several light excitation intensities (Figure 8e,f), one can glean the order of the rate-limiting reaction for loss of charges and therefore, gain information as to the process that limits the yield for electrocatalyst turnover.

Starting with the data in Figure 8c,d, these plots are clearly asymmetric, irrespective of whether the trends in electrocatalyst turnover yield are nearly symmetric (Figure 8a) or asymmetric (Figure 8b). This suggests that the number of charges present at steady-state is not the only indicator of the asymmetry in the trends for turnover yield. The number of steady-state charges reaches a maximum value when both $\tau_{hop(Dye–Dye)}$ and τ_{recomb} are at their maximum value (Figure 8c,d, boundary 1|2), which is not the optimal condition for turnover yield. Irrespective, this condition makes sense because a large value for τ_{recomb} means that recombination is slow and a large value for $\tau_{hop(Dye–Dye)}$ means that a long time is required for an oxidized/reduced dye to encounter an electrocatalyst so that the charge can then be lost due to turnover. Under this condition, turnover

yield is nearly the same as under the optimal condition where instead $\tau_{hop(Dye–Dye)}$ is small (Figure 8a,b). This means that when recombination is slow, hopping does not limit turnover yield, which is a conclusion that is consistent with the analysis of the data in Figure 7a,b.

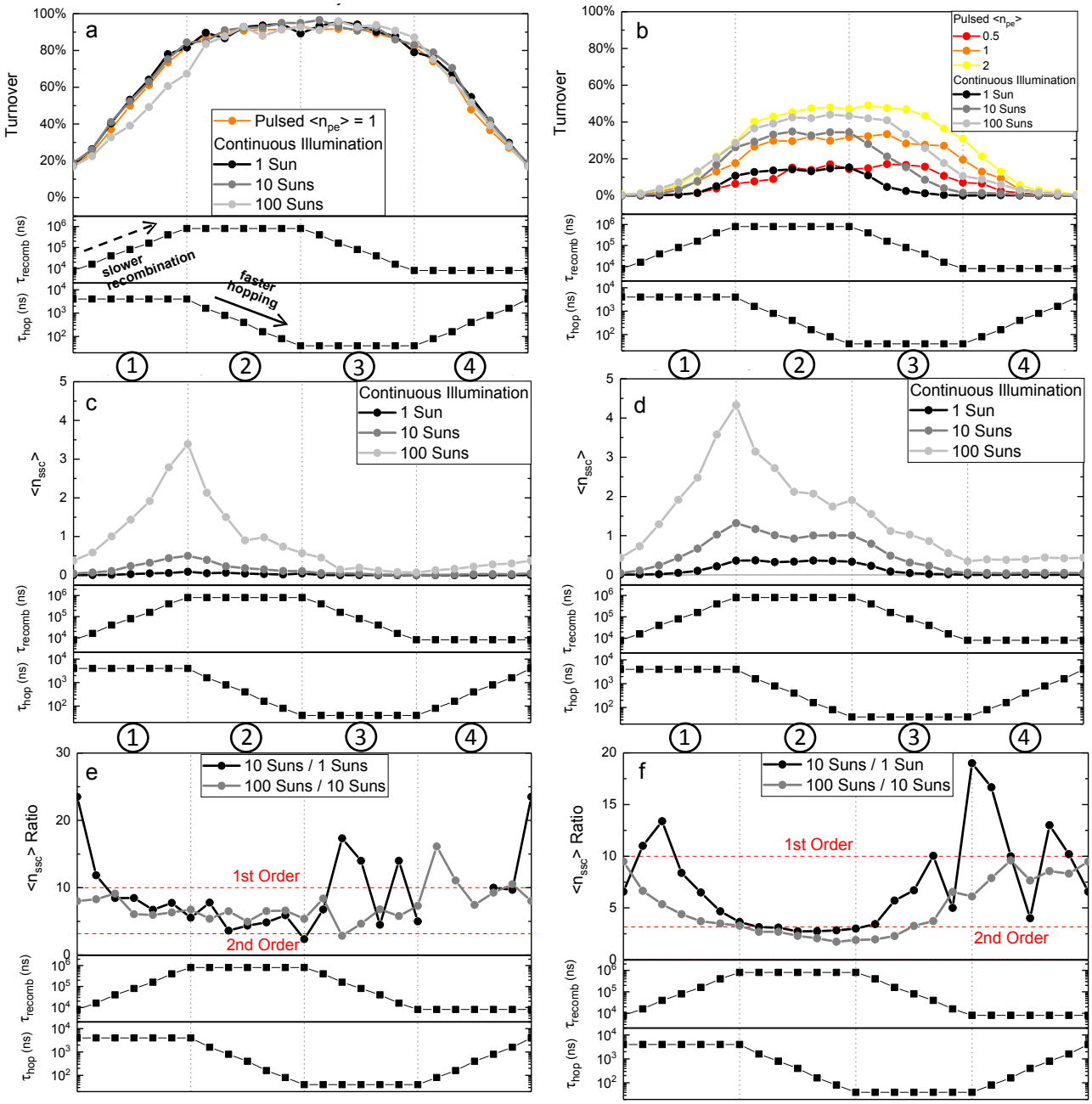

Figure 8. Panoramic plots tracing the perimeter of the parameter spaces covered by the sheet plots in (a) Figure 7a and (b) Figure 7b. As references, panels a and b also contain data from the indicated initial pulsed-light excitation simulations (colored data, taken from Figure 2). Panoramic plots for the conditions in panels a and b showing the average number of molecular charges per particle at steady-state (<n_{ssc}>) as (c, d) raw data and (e, f) normalized to the data obtained using a 10-fold-lower photon fluence, with regions 1, 2, 3, and 4 labeled for all panels.

Before analyzing the trends in the orders of the rate-limiting reactions shown in Figure 8e,f, it is useful to understand how each reaction order is manifest in the data shown in Figure 8e,f and what reaction order is expected for each rate-limiting reaction. Based on Equation 6b, a reaction that is second-order in the number of charges per particle will yield a ratio for the steady-state number of charges per particle of 3.16 and a reaction that is first-order in the number of charges per particle will yield a ratio of 10. In order to determine the reaction order in the number of charges per particle for each kinetic process that results in loss of charge, simulations were performed using initial homogeneous pulsed-light excitation in the presence of only one kinetic process for loss of charge. The rate of recombination was found to exhibit a second-order dependence on $<n_{ssc}>$ due to recombination having a first-order dependence on the number of oxidized/reduced molecules and a first-order dependence on the equal number of charges in the semiconductor nanoparticle (Figure S7a). However, when photon fluence is low such that $<n_{ssc}> \leq 1$, a single recombination event per particle removes all of its charge carriers meaning that each particle only has a binary state of having zero or one charge-separated state and therefore the ensemble average behavior over all particles is in fact first-order in $<n_{ssc}>$ (Figure S7b). This is shown in Figure S7b for the hypothetical scenario when n_{pe} is the same for each particle, and in which case the observed ensemble recombination behavior is second-order in n_{pe} when $<n_{pe}> > 1$, but first-order in n_{pe} when $<n_{pe}> < 1$. Interestingly, the rate of electrocatalyst turnover is approximately first-order in the number of charges per particle over the majority of the charge-separated-state lifetime for the oxidized/reduced dyes (Figure S7c), irrespective of the number of electrocatalysts per particle.

The data in Figure 8e suggest that under all light excitation intensities studied and irrespective of the values of $\tau_{hop(Dye–Dye)}$ and τ_{recomb}, $<n_{ssc}>$ scales nearly linearly with the photon fluence and so the ratio of steady-state charges equals 10. At boundary 0|1, a ratio of 10 is expected because $<n_{ssc}> < 1$ (Figure 8c) and ~80% of the molecular charges are lost due to recombination while the remainder contribute to electrocatalyst turnover (Figure 8a), which is also first-order in number of charges per particle. At boundaries 1|2, 2|3, and 3|4, the ratio of ~10 is expected because >80% of the molecular charges contribute to electrocatalyst turnover (Figure 8a). At boundary 1|2, $<n_{ssc}> > 1$ at high fluence and some particles likely have $n_{scc} > 1$ at low fluence (Figure 8c) and therefore, since < 20% of the molecular charges are lost due to recombination some second-order behavior should be apparent contributing a ratio of ~3, but this in only a minor contribution to the data in Figure 8e. It is challenging to draw additional conclusions from these data due to their near

independence on the time constants or light excitation conditions on the observed behavior, and poor signal-to-noise for the lowest excitation condition. However, this is not the case for electrocatalysts that require two redox events for turnover (Figure 8f).

For electrocatalysts that require two redox events for turnover, all processes that result in the loss of molecular charges require two oxidized/reduced dyes. However, rates of electrocatalyst turnover and rates of recombination when $<n_{ssc}> < 1$ exhibit first-order dependencies in the number of charges (Figure S7b,c). Therefore, it is not surprising that the data in Figure 8f exhibit different ratios for the steady-state number of charges per particle as a function of time constants and light excitation conditions. At boundary 0|1, the ratio of steady-state charges equals ~10, which is expected because at all light excitation intensities, $<n_{ssc}> < 1$ (Figure 8d) and ~100% of the molecular charges are lost due to recombination (Figure 8b). At boundary 1|2, $<n_{ssc}> > 1$ at high fluence and some particles likely have $n_{scc} > 1$ at low fluence (Figure 8d) and therefore, since > 70% of the molecular charges are lost due to recombination, a significant contribution from second-order behavior should be apparent contributing a ratio of ~3 as shown in Figure 8f. This same behavior occurs at boundary 2|3, although at high fluence turnover yield is larger (Figure 8b), and so there is a more significant contribution from the first-order behavior of electrocatalyst turnover. Under this condition, the ratio of steady-state charges equals ~2, which suggests that turnover is larger than second order in the number of charges per particle (Equation 6b) or that the observed rate constant for turnover increases at higher fluences (Equation 4). The data in Figure S7c suggest that for the electrocatalyst coverages and fluences used here, the rate constant does increase considerably, which explains the even lower ratio observed as a global minimum near boundary 2|3 (Figure 8f). Lastly, first-order behavior occurs at boundary 3|4 and boundary 4|0 (Figure 8f), which is expected since turnover yield decreases to < 10% in these regions (Figure 8b).

The consequences of the behavior and limiting mechanisms described above are important in that for the case of electrocatalysts that each require one redox event for turnover, the four boundaries at 1|2, 2|3, 3|4, and 4|0 = 0|1 show drastically different $<n_{ssc}>$ as a function of both illumination intensity and time constants, yet the steady-state number of oxidized/reduced molecules is almost always entirely linear in the photon fluence, with a ratio equal to ~10. This suggests that the fluence-dependence of the rate-limiting recombination reaction is responsible for the symmetric

trends in turnover yield observed for the data shown in Figure 8a. This also helps to explain the minor asymmetry observed at boundary 1|2 under 100 Suns of repeated light excitation where $<n_{pe}> > 1$ and turnover yield only equals ~60%, meaning that second-order recombination with a ratio ~3 occurs for ~40% of the oxidized/reduced molecules. Unfortunately, the signal-to-noise ratio of the data in Figure 8e is too small to definitely observe that trend. This rationale also suggests that the large asymmetric trends in turnover yield observed in Figure 8b are due to the order of the photon fluence on the rate-limiting recombination reaction. For these data, the order of the rate-limiting reaction on $<n_{ssc}>$ ranges from linear (boundary 0|1) to quadratic (boundary 1|2) to linear but with variable rate constant (boundary 2|3) and again to nearly linear (boundary 3|4). The anomalous asymmetry in Figure 8b is most apparent near boundaries 1|2 and 3|4, which are regions that are symmetric in turnover yield behavior at low fluence for electrocatalysts that require a single redox event for turnover (Figure 8a). The asymmetry in turnover yield near these regions and for any simulated fluence with electrocatalysts that require two redox events for turnover is due to second-order recombination-limited loss and partially first-order electrocatalyst turnover loss that dominate near boundary 1|2 in comparison to the predominantly first-order ensemble recombination loss that dominates near boundary 3|4.

The implications of these results are very important for dye-sensitized photoelectrochemical cells and related solar fuels constructs. It is clear that a range of observed kinetic dependencies will occur for the various processes that are operative in dye-sensitized photoelectrochemical materials under constant solar-simulated illumination at 1 – 100 Suns. This means that performing simple kinetic fits to data and analysis of trends will be greatly convoluted by whether each semiconductor nanoparticle has greater than or less than one charge at steady-state. In reality, this behavior is even more complex than reported herein because our models assumed that charges on oxidized/reduced dyes could not transport to other semiconductor particles, that all particles were identical in size, and that there was no distribution in the electronic states in the semiconductor or in the molecular states such that the kinetics could be described by straightforward traditional kinetic rate laws based on the law of mass action. Collectively, these data suggest that kinetic behaviors observed in dye-sensitized photoelectrochemical cells may not be due to heterogeneous environments or non-ideal kinetic processes, but rather the complex interplay of limiting regimes in chemical catalysis that are pertinent to these constructs. Data from these simulations also suggest that, experimentally, kinetics observed using pulsed-laser spectroscopies may represent a

convolution of several traditional kinetic equations even if there is a single underlying kinetic phenomena present. This underscores an even broader conclusion from this study, which is the observation that for electrocatalysts that required multiple redox events for turnover, the conditions of initial pulsed-light excitation could not reproduce the behavior observed based on simulations that mimic the conditions of continuous illumination. Thus, the fundamental time constants for kinetic processes must be obtained using any pulsed-laser fluence but then based on the values obtained, a specific pulsed-laser fluence must be used in order to predict the performance of the materials system under real-world sunlight illumination. This is unfortunate because it requires a larger degree of experimental specificity and interpretation when performing meaningful experiments on these materials systems. For materials systems whose electrocatalysts only require that they are oxidized/reduced once for turnover, a specific laser fluence consistent with exciting approximately one dye per particle should mimic the performance under continuous illumination, assuming the underlying materials geometry, molecular arrangements, and mechanistic kinetic processes used in the models presented herein are accurate for the systems under study. These conclusions are consistent with experimental observations and analyses previously reported in the literature, which are conflicting on the mechanisms, kinetics processes, and even order of reactions in charges that are operative in dye-sensitized photoelectrochemical constructs[45,78,79] and therefore, this remains a very active area of research.

Conclusions

This work developed and reported a new and advanced model for charge transport across dye-sensitized materials that is most pertinent to photoelectrochemical cells for solar fuels constructs. Results from simulations indicate that the largest yields for electrocatalyst turnover occur when the ratio τ_{recomb} / $\tau_{hop(Dye–Dye)}$ is large and that while higher fluences result in larger absolute rates of electrocatalyst turnover, the yields decrease for electrocatalysts that require two oxidations/reductions for turnover. In general, simulation results also suggest that yield for electrocatalyst turnover is largest when the total absorbance of the sample is low or scattering particles are introduced to randomize excitation over the thickness of the nanoparticle stack. Results also suggest that having 1% coverage of electrocatalysts, which equates to ~2.5 electrocatalysts per particle, maximizes the turnover yield for the geometry and parameters

considered in the model. The simulations also show that simulated continuous illumination can be attained through repeated light excitation and in this case observed kinetic behavior can be first-order or second-order in the number of charges per particle, or some linear combination of these processes. Under simulated 1 Sun excitation conditions incorporating dyes used in state-of-the-art dye-sensitized solar cells, on average less than one oxidized/reduced dye is present per particle at steady-state and the purely second-order kinetic processes for recombination results in ensemble first-order kinetic behavior due to the binary redox state of each nanoparticle. This suggests that for effective dye-sensitized photoelectrosynthetic cells for solar fuels production, a low coverage of electrocatalysts is best and depending on the illumination intensity and electron-transfer time constants, yields for electrocatalyst turnover can be quite high under solar-simulated conditions.

Acknowledgements

This work was supported by the National Science Foundation under CHE – 1566160 and the School of Physical Sciences at the University of California Irvine. The authors thank Joseph Cardon for insightful discussions.

References

(1) B. D. James, G. N. Baum, J. Perez, K. N. Baum, DOE Contract Number GS-10F-009J, 2009, 1–128.

(2) Pinaud, B. A.; Benck, J. D.; Seitz, L. C.; Forman, A. J.; Chen, Z.; Deutsch, T. G.; James, B. D.; Baum, K. N.; Baum, G. N.; Ardo, S.; Wang, H.; Miller, E.; Jaramillo, T. F. *Energy Environ. Sci.* **2013**, *6* (7), 1983–2002.

(3) Ager, J. W.; Shaner, M. R.; Walczak, K. A.; Sharp, I. D.; Ardo, S. *Energy Environ. Sci.* **2015**, *8* (10), 2811–2824.

(4) Bala Chandran, R.; Breen, S.; Shao, Y.; Ardo, S.; Weber, A. Z. *Energy Environ. Sci.* **2018**, *11* (1), 115–135.

(5) Ardo, S.; Fernandez Rivas, D.; Modestino, M. A.; Schulze Greiving, V.; Abdi, F. F.;

Alarcon Llado, E.; Artero, V.; Ayers, K.; Battaglia, C.; Becker, J.-P.; Bederak, D.; Berger, A.; Buda, F.; Chinello, E.; Dam, B.; Di Palma, V.; Edvinsson, T.; Fujii, K.; Gardeniers, H.; Geerlings, H.; H. Hashemi, S. M.; Haussener, S.; Houle, F.; Huskens, J.; James, B. D.; Konrad, K.; Kudo, A.; Kunturu, P. P.; Lohse, D.; Mei, B.; Miller, E. L.; Moore, G. F.; Muller, J.; Orchard, K. L.; Rosser, T. E.; Saadi, F. H.; Schüttauf, J.-W.; Seger, B.; Sheehan, S. W.; Smith, W. A.; Spurgeon, J.; Tang, M. H.; van de Krol, R.; Vesborg, P. C. K.; Westerik, P. *Energy Environ. Sci.* **2018**, *11* (10), 2768–2783.

(6) Verlage, E.; Hu, S.; Liu, R.; Jones, R. J. R.; Sun, K.; Xiang, C.; Lewis, N. S.; Atwater, H. A. *Energy Environ. Sci.* **2015**, *8* (11), 3166–3172.

(7) Jia, J.; Seitz, L. C.; Benck, J. D.; Huo, Y.; Chen, Y.; Ng, J. W. D.; Bilir, T.; Harris, J. S.; Jaramillo, T. F. *Nat. Commun.* **2016**, *7* (May), 1–6.

(8) Schüttauf, J.-W.; Modestino, M. A.; Chinello, E.; Lambelet, D.; Delfino, A.; Dominé, D.; Faes, A.; Despeisse, M.; Bailat, J.; Psaltis, D.; Moser, C.; Ballif, C. *J. Electrochem. Soc.* **2016**, *163* (10), F1177–F1181.

(9) Zhou, X.; Liu, R.; Sun, K.; Chen, Y.; Verlage, E.; Francis, S. A.; Lewis, N. S.; Xiang, C. *ACS Energy Lett.* **2016**, *1* (4), 764–770.

(10) Young, J. L.; Steiner, M. A.; Döscher, H.; France, R. M.; Turner, J. A.; Deutsch, T. G. *Nat. Energy* **2017**, *2* (4), 1–8.

(11) Yuvraj, S. *Modeling and experimental demonstration of an integrated photoelectrochemical hydrogen generator working under concentrated irradiation*, École Polytechnique Fédérale de Lausanne, Thesis, 2018.

(12) Li, F.; Yang, H.; Li, W.; Sun, L. *Joule* **2018**, *2* (1), 36–60.

(13) Kudo, A.; Miseki, Y. *Chem. Soc. Rev.* **2009**, *38* (1), 253–278.

(14) Alibabaei, L.; Brennaman, M. K.; Norris, M. R.; Kalanyan, B.; Song, W.; Losego, M. D.; Concepcion, J. J.; Binstead, R. a.; Parsons, G. N.; Meyer, T. J. *Proc. Nat. Acad. Sci. USA* **2013**, *110*, 20008–20013.

(15) Lin, F.; Boettcher, S. W. *Nat. Mater.* **2014**, *13* (1), 81–86.

(16) Warren, E. L.; Atwater, H. A.; Lewis, N. S. *J. Phys. Chem. C* **2014**, *118* (2), 747–759.

(17) Yu, Z.; Li, F.; Sun, L. *Energy Environ. Sci.* **2015**, *8* (3), 760–775.

(18) Zandi, O.; Hamann, T. W. *Nat. Chem.* **2016**, *8* (8), 778–783.

(19) Kalisman, P.; Nakibli, Y.; Amirav, L. *Nano Lett.* **2016**, *16* (3), 1776–1781.

(20) Kim, H. J.; Kearney, K. L.; Le, L. H.; Haber, Z. J.; Rockett, A. A.; Rose, M. J. *J. Phys. Chem. C* **2016**, *120* (45), 25697–25708.

(21) Utterback, J. K.; Grennell, A. N.; Wilker, M. B.; Pearce, O. M.; Eaves, J. D.; Dukovic, G. *Nat. Chem.* **2016**, *8* (11), 1061–1066.

(22) Pekarek, R. T.; Kearney, K.; Simon, B. M.; Ertekin, E.; Rockett, A. A.; Rose, M. J. *J. Am. Chem. Soc.* **2018**, *140* (41), 13223–13232.

(23) Wadsworth, B. L.; Khusnutdinova, D.; Moore, G. F. *J. Mater. Chem. A* **2018**, *6* (44), 21654–21665.

(24) Osterloh, F. E. *Chem. Soc. Rev.* **2013**, *42* (6), 2294–2320.

(25) Fabian, D. M.; Hu, S.; Singh, N.; Houle, F. A.; Hisatomi, T.; Domen, K.; Osterloh, F. E.; Ardo, S. *Energy Environ. Sci.* **2015**, *8* (10), 2825–2850.

(26) Maeda, K.; Domen, K. *J. Phys. Chem. Lett.* **2010**, *1* (18), 2655–2661.

(27) Hisatomi, T.; Kubota, J.; Domen, K. *Chem. Soc. Rev.* **2014**, *43* (22), 7520–7535.

(28) Wrighton, M. S. *Acc. Chem. Res.* **1979**, *12* (9), 303–310.

(29) Dominey, R. N.; Lewis, N. S.; Bruce, J. A.; Bookbinder, D. C.; Wrighton, M. S. *J. Am. Chem. Soc.* **1982**, *104* (2), 467–482.

(30) Moore, G. F.; Blakemore, J. D.; Milot, R. L.; Hull, J. F.; Song, H.; Cai, L.; Schmuttenmaer, C. A.; Crabtree, R. H.; Brudvig, G. W. *Energy Environ. Sci.* **2011**, *4* (7), 2389.

(31) Foley, J. M.; Price, M. J.; Feldblyum, J. I.; Maldonado, S. *Energy Environ. Sci.* **2012**, *5* (1), 5203–5220.

(32) Haussener, S.; Xiang, C.; Spurgeon, J. M.; Ardo, S.; Lewis, N. S.; Weber, A. Z. *Energy Environ. Sci.* **2012**, *5* (12), 9922–9935.

(33) Mills, T. J.; Lin, F.; Boettcher, S. W. *Phys. Rev. Lett.* **2014**, *112* (14), 148304.

(34) Singh, M. R.; Haussener, S.; Weber, A. Z. 2019; pp 500–536.

(35) Papageorgiou, N.; Grätzel, M.; Infelta, P. P. *Sol. Energy Mater. Sol. Cells* **1996**, *44* (4), 405–438.

(36) Papageorgiou, N.; Barbe, C.; Gratzel, M. *J. Phys. Chem. B* **1998**, *102* (21), 4156–4164.

(37) Bonhôte, P.; Gogniat, E.; Tingry, S.; Barbé, C.; Vlachopoulos, N.; Lenzmann, F.; Comte, P.; Grätzel, M. *J. Phys. Chem. B* **1998**, *102* (9), 1498–1507.

(38) Papageorgiou, N.; Liska, P.; Kay, A.; Grätzel, M. *J. Electrochem. Soc.* **1999**, *146* (3), 898–907.

(39) Bisquert, J. *J. Phys. Chem. B* **2002**, *106* (2), 325–333.

(40) Papageorgiou, N. *Coord. Chem. Rev.* **2004**, *248* (13–14), 1421–1446.

(41) Bisquert, J. *J. Phys. Chem. C* **2007**, *111* (46), 17163–17168.

(42) Ansari-Rad, M.; Anta, J. A.; Bisquert, J. *J. Phys. Chem. C* **2013**, *117* (32), 16275–16289.

(43) Gonzalez-Vazquez, J. P.; Oskam, G.; Anta, J. A. *J. Phys. Chem. C* **2012**, *116* (43), 22687–22697.

(44) Anta, J. A.; Casanueva, F.; Oskam, G. *J. Phys. Chem. B* **2006**, *110* (11), 5372–5378.

(45) Ardo, S.; Meyer, G. J. *Chem. Soc. Rev.* **2009**, *38* (1), 115–164.

(46) Hagfeldt, A.; Boschloo, G.; Sun, L.; Kloo, L.; Pettersson, H. *Chem. Rev.* **2010**, *110* (11), 6595–6663.

(47) Hu, K.; Meyer, G. J. *Langmuir* **2015**, *31* (41), 11164–11178.

(48) Trammell, S. A.; Yang, J.; Sykora, M.; Fleming, C. N.; Odobel, F.; Meyer, T. J. *J. Phys. Chem. B* **2001**, *105* (37), 8895–8904.

(49) Nelson, J. *Phys. Rev. B* **1999**, *59* (23), 15374–15380.

(50) Nelson, J.; Haque, S. A.; Klug, D. R.; Durrant, J. R. *Phys. Rev. B* **2001**, *63* (20), 205321.

(51) Nelson, J.; Chandler, R. E. *Coord. Chem. Rev.* **2004**, *248* (13–14), 1181–1194.

(52) Vaissier, V.; Mosconi, E.; Moia, D.; Pastore, M.; Frost, J. M.; De Angelis, F.; Barnes, P. R. F.; Nelson, J. *Chem. Mater.* **2014**, *26* (16), 4731–4740.

(53) Wang, Q.; Ito, S.; Grätzel, M.; Fabregat-Santiago, F.; Mora-Seró, I.; Bisquert, J.; Bessho, T.; Imai, H. *J. Phys. Chem. B* **2006**, *110* (50), 25210–25221.

(54) Anta, J. A.; Nelson, J.; Quirke, N. *Phys. Rev. B - Condens. Matter Mater. Phys.* **2002**, *65* (12), 1–10.

(55) Wang, Q.; Moser, J.; Grätzel, M. *J. Phys. Chem. B* **2005**, *109* (31), 14945–14953.

(56) Gao, F.; Wang, Y.; Shi, D.; Zhang, J.; Wang, M.; Jing, X.; Humphry-Baker, R.; Wang, P.; Zakeeruddin, S. M.; Grätzel, M. *J. Am. Chem. Soc.* **2008**, *130* (32), 10720–10728.

(57) Trammell, S. A.; Meyer, T. J. *J. Phys. Chem. B* **1999**, *103* (1), 104–107.

(58) Ardo, S.; Meyer, G. J. *J. Am. Chem. Soc.* **2010**, *132* (27), 9283–9285.

(59) Ardo, S.; Sun, Y.; Staniszewski, A.; Castellano, F. N.; Meyer, G. J. *J. Am. Chem. Soc.* **2010**, *132* (19), 6696–6709.

(60) Chen, H.; Ardo, S. *Nat. Chem.* **2017**, *10* (1), 17–23.

(61) Moia, D.; Szumska, A.; Vaissier, V.; Planells, M.; Robertson, N.; O'Regan, B. C.; Nelson, J.; Barnes, P. R. F. *J. Am. Chem. Soc.* **2016**, *138* (40), 13197–13206.

(62) Ardo, S. *Photoinduced Charge, Ion & Energy Transfer Processes at Transition-Metal Coordination Compounds Anchored to Mesoporous, Nanocrystalline Metal-Oxide Thin Films*, Johns Hopkins University, Thesis, 2010.

(63) Barzykin, A. V.; Tachiya, M. *J. Phys. Chem. B* **2002**, *106* (17), 4356–4363.

(64) Katoh, R.; Furube, A.; Barzykin, A. V.; Arakawa, H.; Tachiya, M. *Coord. Chem. Rev.* **2004**, *248* (13–14), 1195–1213.

(65) Barzykin, A. V.; Tachiya, M. *J. Phys. Chem. B* **2004**, *108* (24), 8385–8389.

(66) Higgins, G. T.; Bergeron, B. V.; Hasselmann, G. M.; Farzad, F.; Meyer, G. J. *J. Phys. Chem. B* **2006**, *110* (6), 2598–2605.

(67) Hu, K.; Robson, K. C. D.; Beauvilliers, E. E.; Schott, E.; Zarate, X.; Arratia-Perez, R.; Berlinguette, C. P.; Meyer, G. J. *J. Am. Chem. Soc.* **2014**, *136* (3), 1034–1046.

(68) Anta, J. A.; Mora-Seró, I.; Dittrich, T.; Bisquert, J. *Phys. Chem. Chem. Phys.* **2008**, *10* (30), 4478.

(69) Anta, J. A. *Energy Environ. Sci.* **2009**, *2* (4), 387.

(70) Anta, J. A.; Morales-Flórez, V. *J. Phys. Chem. C* **2008**, *112* (27), 10287–10293.

(71) Brennan, B. J.; Durrell, A. C.; Koepf, M.; Crabtree, R. H.; Brudvig, G. W. *Phys. Chem. Chem. Phys.* **2015**, *17* (19), 12728–12734.

(72) Brennan, B. J.; Regan, K. P.; Durrell, A. C.; Schmuttenmaer, C. A.; Brudvig, G. W. *ACS Energy Lett.* **2017**, *2* (1), 168–173.

(73) Rettie, A. J. E.; Chemelewski, W. D.; Emin, D.; Mullins, C. B. *J. Phys. Chem. Lett.* **2016**, *7* (3), 471–479.

(74) Ardo, S.; Meyer, G. J. *J. Am. Chem. Soc.* **2011**, *133* (39), 15384–15396.

(75) O'Regan, B. C.; Durrant, J. R. *Acc. Chem. Res.* **2009**, *42* (11), 1799–1808.

(76) Askerka, M.; Brudvig, G. W.; Batista, V. S. *Acc. Chem. Res.* **2017**, *50* (1), 41–48.

(77) Ashford, D. L.; Gish, M. K.; Vannucci, A. K.; Brennaman, M. K.; Templeton, J. L.; Papanikolas, J. M.; Meyer, T. J. *Chem. Rev.* **2015**, *115* (23), 13006–13049.

(78) Xu, P.; Gray, C. L.; Xiao, L.; Mallouk, T. E. *J. Am. Chem. Soc.* **2018**, *140* (37), 11647–11654.

(79) Brigham, E. C.; Meyer, G. J. *J. Phys. Chem. C* **2014**, *118* (15), 7886–7893.